

Using deep learning to detect patients at risk for prostate cancer despite benign biopsies

Boing Liu¹, Yinxi Wang¹, Philippe Weitz¹, Johan Lindberg¹, Lars Egevad², Henrik Grönberg¹, Martin Eklund¹,
Mattias Rantalainen^{1,*}

¹Department of Medical Epidemiology and Biostatistics, Karolinska Institutet, Stockholm, Sweden

²Department of Oncology-Pathology, Karolinska Institutet, Stockholm, Sweden

* Corresponding author: mattias.rantalainen@ki.se

Keywords: computational pathology, prostate cancer, deep learning, histopathology

Abstract

Background: Transrectal ultrasound guided systematic biopsies of the prostate is a routine procedure to establish a prostate cancer diagnosis. However, the 10-12 prostate core biopsies only sample a relatively small volume of the prostate, and tumour lesions in regions between biopsy cores can be missed, leading to a well-known low sensitivity to detect clinically relevant cancer. As a proof-of-principle, we developed and validated a deep convolutional neural network model to distinguish between morphological patterns in benign prostate biopsy whole slide images from men with and without established cancer.

Methods: This study included 14,354 hematoxylin and eosin stained whole slide images from benign prostate biopsies from 1,508 men in two groups: men without an established prostate cancer (PCa) diagnosis and men with at least one core biopsy diagnosed with PCa. 80% of the participants were assigned as training data and used for model optimization (1,211 men), and the remaining 20% (297 men) as a held-out test set used to evaluate model performance. An ensemble of 10 deep convolutional neural network models was optimized for classification of biopsies from men with and without established cancer. Hyperparameter optimization and model selection was performed by cross-validation in the training data.

Results: Area under the receiver operating characteristic curve (ROC-AUC) was estimated as 0.727 (bootstrap 95% CI: 0.708-0.745) on biopsy level and 0.738 (bootstrap 95% CI: 0.682 - 0.796) on man level. At a specificity of 0.9 the model had an estimated sensitivity of 0.348.

Conclusion: The developed model has the ability to detect men with risk of missed PCa due to under-sampling of the prostate. The proposed model has the potential to reduce the number of false negative cases in routine systematic prostate biopsies and to indicate men who could benefit from MRI-guided re-biopsy.

Introduction

Prostate cancer (PCa) is the second most common cancer (after lung cancer) in men worldwide¹ and the most common form of cancer in Sweden². Transrectal ultrasound (TRUS) guided 10-12 core needle prostate biopsy is the most common diagnostic tool for men who have elevated prostate-specific antigen (PSA) and/or abnormal digital rectal examination (DRE) and/or other suspicious indications³. A major limitation of the systematic TRUS prostate biopsy is undersampling, causing cancer lesions between biopsy cores to be missed⁴. Consequently, the sensitivity of TRUS guided systematic biopsy has been reported as low as 32-58%^{5,6} and increasing the number of biopsy cores only marginally improves the sensitivity and mainly detects indolent cancers⁷. Although magnetic resonance (MRI)-guided targeted biopsy is recommended for biopsy naive patients and patients with indications for repeated biopsy, it is currently not widely available to patients on a broad scale. Improvements in the sensitivity of TRUS biopsy, especially for more aggressive PCa, is therefore warranted to improve the detection of clinically relevant cancer and to reduce unnecessary rebiopsies, which ultimately benefits patient outcomes.

PCa diagnosis based on histopathological inspection of prostate biopsy (hematoxylin-eosin [H&E] stained) slides is challenging and prone to inter-assessor variability^{4,8}. So far, there are only three features (i.e. perineural invasion, glomerulations, and mucinous fibroplasia) that have not been observed in benign prostate glands and therefore are considered to be diagnostic for PCa. On the other hand, most PCa are identified based on a combination of non-specific major and minor cancer architectural and cytological features⁴. The major features (eg. infiltrative growth pattern, absence of basal cells, and nuclear atypia) are strongly linked to cancer, while the minor features (eg. cytoplasmic amphophilia, intraluminal contents, mitosis and apoptosis) are less strongly linked to cancer, and can both be seen in non-cancer lesions⁴. In addition, premalignant changes of high-grade prostatic intraepithelial neoplasia (HGPIN) and atypical small acinar proliferation (ASAP) are associated with later prostate cancer diagnosis⁴. It is well recognized that development of cancer is a continual process in which cells gradually become malignant as a result of the accumulation of mutations and selection⁹. Moreover, epigenetic changes have been reported in the early development of cancer and distinct epigenetic signatures may be present in neighbouring prostatic tissues adjacent to the PCa foci¹⁰. Therefore, subtle cancer-related morphological structures with clinical relevance, which are either non-specific or not detectable by human eyes, could present in benign cores sampled in the vicinity of the cancer areas.

Deep learning (DL)¹¹ in the form of convolutional neural networks currently offers state-of-the-art methodologies for representation learning and image classification. Applications of DL for modelling of histopathology images have recently demonstrated that models can achieve human level image classification performance in routine pathology assessments tasks¹², including cancer detection and grading^{13,14}. DL has also demonstrated capacity to extract information that allows the prediction of factors from H&E stained WSIs, which are not possible to be determined in conventional routine pathology by a human assessor, including status of molecular markers^{15,16} and microsatellite instability¹⁷. Consequently, we can hypothesize that there are also other subtle morphological patterns present in images of stained histopathology sections that potentially could be exploited by DL approaches, which enables prediction and classification of other clinically relevant factors. In this study, we investigate the potential to apply DL models that can recognise cancer-associated morphological changes in benign biopsies, with a focus on assessing to what extent such models could be used to improve sensitivity to detect clinically relevant cancer in TRUS guided systematic prostate biopsies.

Methods

Study population

The study was based on a subset of men from the STHLM3 study¹⁸. STHLM3 is a prospective population-based diagnostic study for PCa conducted between May 2012 and Dec 2014. The study enrolled a random sample of men aged between 50 and 69 years who were free of promoted PCa from the Swedish population register. Out of those, 59,159 men accepted to participate in the study¹⁸. 7,406 (12.5%) men underwent TRUS prostate biopsies (10-12 cores), which were reviewed and graded according to the International Society of Urological Pathology (ISUP)¹⁹ system by a single pathologist (Lars Egevad). The study population was made of 606 men with detected cancer (ISUP \geq 1) randomly sampled together with 134 men with only benign biopsies from STHLM3, for details see¹³, all benign biopsies from these 740 men were included in the present study. To further increase the number of men with only benign biopsies in the study, all benign biopsies from subjects enrolled during 2015 in STHLM3 (N=877 men, 585 benign, 292 cancer) were digitized and included in the present analysis.

To reduce potential labeling error, we excluded participants or biopsies if there were errors in GS (i.e. duplicates with inconsistent patient level gleason score), cancer diagnosis, cancer length, as well as all cancerous biopsies graded as GS 3+3 or above (**eFigure 1**). Data missing in PSA and age was not included in the analysis (**eFigure 1**).

After applying the exclusion criteria, in total, we collected 14,354 benign biopsies from 829 men (6523 biopsies) with detected cancer (at least one core biopsy had cancer detected by pathologist) (cancer-benign biopsies), and 679 men (7831 biopsies) with no detected cancer (all cores classified as benign by pathologist) (benign-benign biopsies) (**eFigure 1**). All prostate biopsy whole slide images (WSI) were digitized at 20X magnification (pixel size 0.4536 μm) on a Hamamatsu Nanozoomer XR histopathology scanner. The data were randomly split on the patient level into training (973 men), validation (238 men), and held out test (297 men) sets. The split (i.e. training and validation versus held out test) was balanced on age, PSA levels, and cancer diagnosis. For cancer patients, the split was further balanced on ISUP grade and the length of the cancer area in the respective biopsy.

Data pre-processing

Tissue segmentation and image tiling

WSIs were read using OpenSlide²⁰. To determine the location of tissue in the WSI, WSIs were transformed from red-green-blue (RGB) to hue-saturation-value (HSV) color space. Binary tissue masks were then generated using the Otsu threshold²¹ of the saturation and a cut-off value of 0.75 for the hue in the HSV color space. A Laplacian filtering algorithm was subsequently applied to separate tissue from pen mark annotations. The tissue masks were further smoothed by applying a morphological opening and closing, with a disk with a radius of 6 to remove salt and pepper noise from the masks (see Supplementary Methods Image preprocessing for details). Tissue areas were subsequently downsampled by a factor of 2 (10X magnification level, pixel size approximate 0.90 μm) and the WSIs were split into image tiles of size 299 by 299 pixels, with 50% overlap. In total, we obtained 8,780,026 image tiles for training, 2,192,124 for validation, and 2,713,314 for the test set.

Image classification

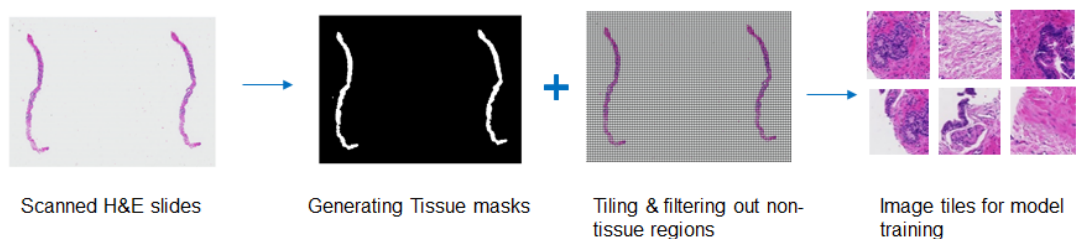
We applied a deep convolutional neural network model based on the ResNet18 architecture^{22,23} to predict a binary outcome of benign biopsy cores from benign men versus benign biopsy cores from men with detected cancer, using preprocessed image tiles together with age and PSA level. Age was categorised in five groups ≤ 55 , 55-60, 60-65, 65-70, 70-100 years. PSA level at the biopsy was grouped as 1-3, 3-5, 5-10, ≥ 10 ng/ml.

The model was optimised using training and validated using validation data (Supplementary materials: Model training) as a weakly supervised binary classification problem, where the patient-level class is assigned to each tile. In total, 8,780,026 tiles for training, 2,192,124 for validation and 2,713,314 for testing were available. The weights

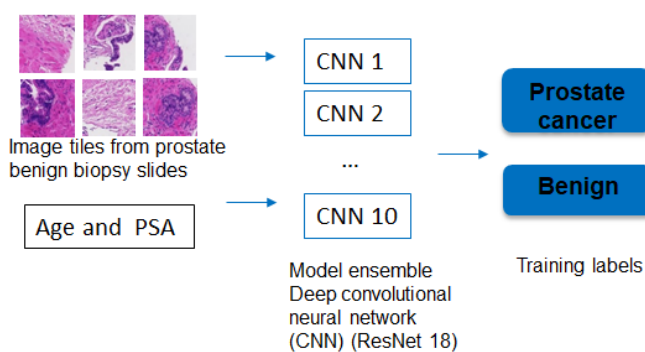
in the model were initialized from a model pre-trained by the ImageNet database²⁴. Optimization was performed by back-propagation, binary cross entropy loss, and the Adam optimizer²⁵. We applied 50% drop-out after global-average-pooling of the final feature maps as well as 50% drop-out and max-norm regularization²⁶ in the last fully connected layer of the model to mitigate potential over-fitting (Supplementary materials: Model overview).

Hyper-parameters were optimized using five-fold cross-validation in the training set, including tile size, magnification level, and learning rate. Finally, to reduce variance in predictions further, the final model is an ensemble of 10 CNN models. See **Figure 1** for an overview of the modelling methodology. Classification performance was evaluated in the held-out test set using Receiver Operating Characteristics (ROC) and Area Under the ROC curve (AUC), and 95% confidence intervals for AUC were obtained using bootstrap (2,000 bootstrap samples). The slide level predictions were aggregated using the 75th percentile of the predicted class probabilities across all tiles from each WSI and patient level predictions were based on the median across all WSI level predictions of an individual. Percentiles for tile-to-slide and slide-to-patient aggregations were optimized using five-fold cross validation. Sensitivity for detecting cancer patients was evaluated at specificity levels of 0.99, 0.95, and 0.90. Computations were performed on a server with four Nvidia RTX 2080 Ti graphics processing unit (GPU) cards. Images were imported to the Python environment using OpenSlide (v. 1.1.1). Convolutional neural networks were implemented in Python 3.6.4 using Keras (v. 2.2.4) with TensorFlow (v. 1.11.0) backend.

a. Data pre-processing



b. Training CNN and optimize hyperparameters



c. Prostate biopsy

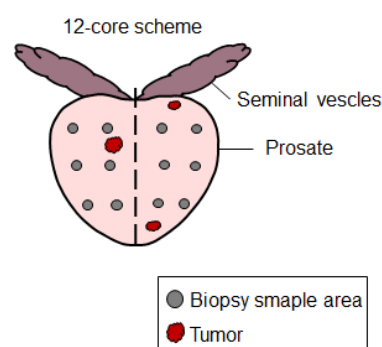


Figure 1. Overview of image pre-processing and DL modelling for detecting cancer patients from benign prostate biopsies only. a) Pre-processing of WSIs. b) Schematic overview of the image classification by a deep CNN ensemble. c) Systematic prostate biopsy 12-core scheme.

Model Interpretation

Guided gradient-weighted class activation mapping (Guided Grad-CAM)

We applied guided gradient-weighted class activation mapping (Guided Grad-CAM)^{26,27} to visualize salient morphological features underlying the DL based prediction. The guided grad-cams were generated based on the best performed model (i.e. highest AUC) among the ten ensemble models. We calculated the gradients of cancer with respect to the 8 by 8 feature map activations from the last convolutional layer (ie. $8 \times 8 \times 512$ dimension). The gradients for each 8 by 8 feature map were global-average-pooled to obtain feature-map-specific weights. The weighted linear combination of the 512 forward activation maps was followed by a ReLU function to obtain an 8 by 8 coarse heatmap. This heatmap was further up-sampled and interpolated to the corresponding image tile size (299 by 299 pixels) to visualize morphological features that were potentially linked to prostate cancer.

Uniform Manifold Approximation and Projection (UMAP) for dimension reduction and visualisation

We randomly selected 20% benign tiles from cancer patients and benign tiles from healthy patients from the test set and applied UMAP²⁸ to generate a two-dimensional representation of the 512-dimensional feature vector learned in the DL model. Based on the UMAP representation, we arbitrarily selected four distinct regions for cancer-benign and benign-benign groups, respectively, for visualisation of representative samples of tiles. For each region, we sampled 16 cancer-benign tiles with highest predicted score and 16 benign-benign tiles with the lowest predicted score to generate the guided grad-cam that illustrates morphological structures associated with the predicted outcome.

Results

An ensemble of 10 deep CNN models for binary classification of benign prostate biopsies from benign-only men and men with diagnosed prostate cancer was optimised based on 9,192 prostate biopsy WSIs (8,780,026 tiles) from 973 men (535 cancer, 438 benign) after applying the exclusion criteria. The classification performance of the ensemble CNN model was then estimated in the validation set (238 men [130 cancer, 108 benign], 2,311 WSIs, 2,192,124 tiles) and subsequently evaluated in the independent held out test dataset (297 men [164 cancer, 133 benign], 2851 WSIs, 2,713,314 tiles) (**Figure 2a** - ROC curve). We observed a tile level prediction performance of AUC=0.701 (bootstrap 95% CI: 0.700 - 0.701), slide level AUC=0.727 (bootstrap 95% CI: 0.708-0.745), and a

patient level AUC=0.738 (bootstrap 95% CI: 0.682 - 0.796). Based on the patient level analysis, we assessed prediction performance for specificity of 0.99, 0.95, and 0.90. (**Figure 2b**). For cancer detection, we observed the sensitivity of 0.043 at the specificity of 0.99, and the sensitivity of 0.224 at specificity of 0.95, and the sensitivity of 0.348 at the specificity of 0.90. These sensitivities differed by ISUP groups with a trend towards higher sensitivity for more aggressive cancers graded as ISUP 4 or 5 (**Figure 2b** and **eTable 1**). We also applied logistic regression to evaluate baseline prediction performance using only age and PSA as the predictors and observed an AUC of 0.562 (bootstrap 95% CI: 0.510 - 0.612) in the held-out test set.

To provide further characterization and interpretation of the CNN model, we applied UMAP to generate a 2-D projection of the 512 high dimensional feature vectors learned in the CNN. The 2-D manifold projection was able to separate benign tiles from men without PCa and benign tiles from men with PCa to a certain extent, indicated by clear difference in tile densities in the UMAP projects of each class (**Figure 3 a & b** middle plots). Image tiles from different selected regions in UMAPs show differences in morphological features. We applied the gradient-based approach, guided Grad-Cam^{26,27}, to further visualize the indicative areas in the tiles linked to cancer associated morphological patterns. As expected, benign tiles from men with benign diagnosis (**Figure 3a**) generally had fewer areas and weaker indication by the Grad-Cam method, while more and larger areas, and with stronger indication, in the benign tiles from PCa men (**Figure 3b**) were highlighted by the guided Grad-Cam.

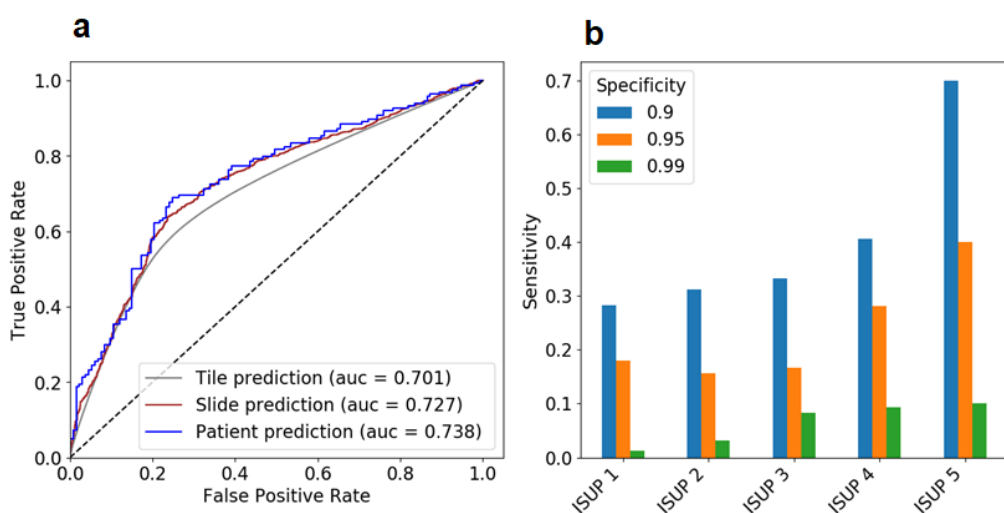


Figure 2. Prediction performance in held-out test set a) Receiver Operating Characteristic (ROC) curves and associated AUC estimates in the hold-out test set for prediction of cancer versus benign PCa diagnosis on tile, slide, and patient level; b) corresponding sensitivity by ISUP group at specificities of 0.99, 0.95, and 0.90.

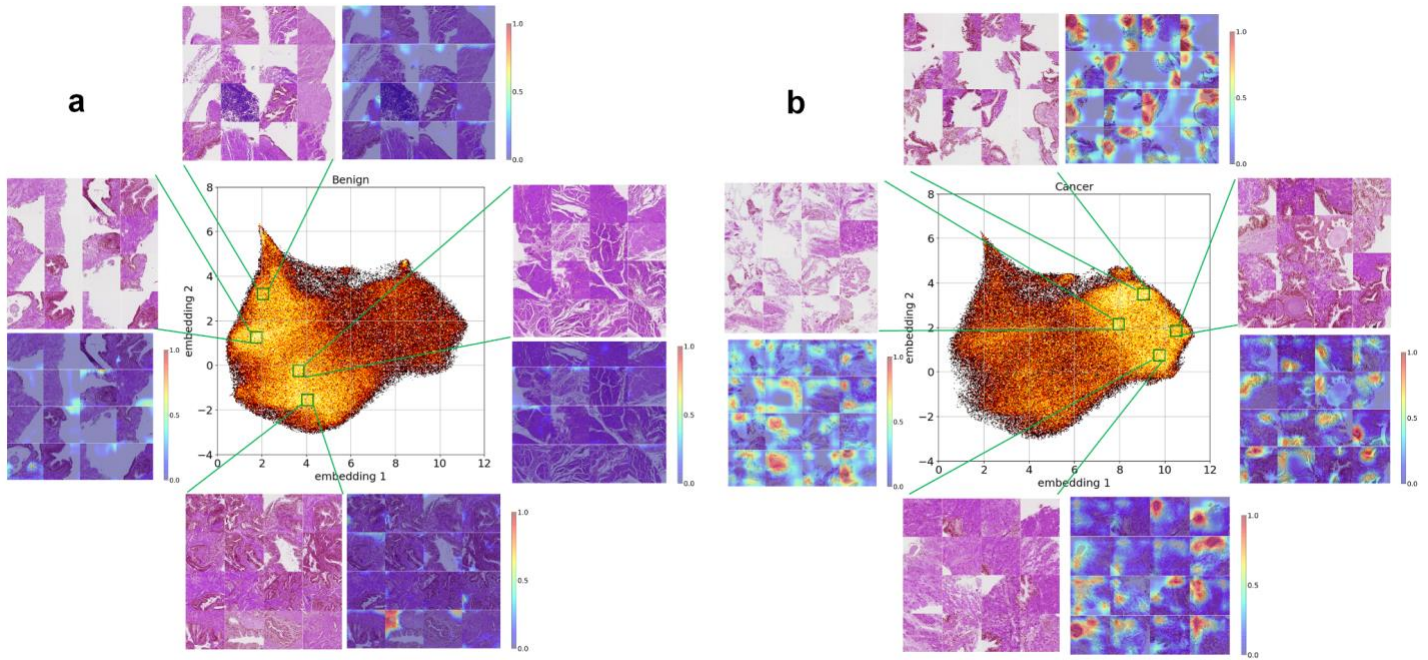


Figure 3. Model characterization and interpretation using UMAP and gradcam a) UMAP projection of benign tiles from men with benign diagnosis (middle). Examples of benign tiles and corresponding grad-cams (outside) from four distinct regions from the UMAP. b) UMAP projection of benign tiles from men with PCa diagnosis (middle). Examples of benign tiles and corresponding grad-cams (outside) from four distinct regions from the UMAP. The two-dimensional plots are reduced from 512-dimensional feature maps from the last fully connected layer.

Discussion

In this study we developed a DL-based model for classification of WSIs of benign prostate core biopsies from men without a cancer diagnosis and from men with at least one biopsy core with cancer. The model achieved a patient level AUC of 0.738, and given at a specificity level of 0.90, the proposed model was able to detect 34.8% of all PCa, and 41% ISUP 4 and 70% of ISUP 5 PCa, from benign biopsy cores only.

There is a plethora of challenges associated with PCa detection by biopsy. PCa is often multifocal and samples taken by systematic TRUS biopsy sample a relatively small volume of the prostate, hence, there is an intrinsic and substantial risk that biopsy cores miss a cancer lesion²⁹. The peripheral zone that harbors 70-80% of the PCa are most frequently sampled, while the transition zone which contains 20% of the cancers is typically not sampled during the initial biopsy⁴. In addition, the biopsy sampling template in clinical practice may vary substantially, a Swedish study based on 137 urologists reported that one third of the urologists never or seldomly sampled the anterior part of the prostate (in the peripheral zone)³⁰ despite its high cancer frequency³¹. The possible false

negatives from the initial biopsy warrants repeated biopsies for patients with abnormal DRE or continuously increased PSA or PSA derivatives. However, due to the nonspecificity of these indicators, cancer detection rate for the second biopsy under the saturation protocol (≥ 20 cores) remains low (22-24%)^{32,33} as compared to the initial 10-12 core biopsy (22.8 -37.2%)^{34,35}. In fact, multiple re-biopsies may be performed before establishing a PCa diagnosis⁷. The procedure causes patients' anxiety and potential side effects⁷. Although rare, repeat biopsies pose increased risk of infection and sepsis due to bacterial colonization in the rectum and the probability of sepsis after the biopsy has been conventionally estimated at 1-3%⁷.

Our DL model was able to identify 34.8 % of the prostate cancer cases at a specificity of 0.90, among which 70% of the ISUP 5 and 41% of the ISUP 4 cases were detected based on only benign biopsies from these cases. This suggests that there are distinct, albeit subtle, morphological differences between benign prostate tissue in men with cancer present in the prostate (adjacent, or nearby) and men without any cancer present. These subtle differences could be captured by image analysis using deep convolutional neural networks but are not captured in routine histopathology assessments by human assessors. A high predicted risk score from a computer model could thus potentially assist pathologists, and indicate either further review of the histopathology slides, or guide decision for re-biopsy. It is further interesting to note that our model showed higher sensitivity for more aggressive PCa (ISUP 4 and 5) as compared to low-to-medium risk PCa, although under-sampling of cancerous tissue may be less prevalent in poor differentiated PCa as larger volume tumours are more often seen in more advanced GS patterns³⁶. The PSA-based screening and subsequent biopsy reduce the prostate-specific mortality, it however leads to overtreatment of low-risk cancer (ISUP 1)³⁷. In fact, 50% of men diagnosed by systematic biopsy have indolent low-risk PCa³⁸, which may only require active surveillance rather than immediate intervention³⁹. The model implemented here appears to have desirable properties in that it contributes to the identification of high risk PCa cases missed due to sparse sampling of the prostate during biopsy, while it detects low risk PCa (low ISUP) at lower rate, thus not driving the risk of additional over-treatment. Despite previous success of deep learning in detection of cancer, cancer grading, and determination of cancer length and prognostic indicators^{13,14,40-42}, there have been few attempts to extract additional information beyond what human assessors can detect from WSIs. We provide the first evidence that deep CNN models can distinguish between benign biopsies from men with established cancer, and benign biopsies from men with only benign biopsies.

The study has several strengths. The study included a large sample size of 15,231 slides from 1,605 men. Slides included in the study were scanned from a single histopathology scanner model, precluding potential bias due to use of different scanning devices, in different subpopulations of patients. Data from the current study was part of the well-controlled STHLM 3 population-based study. The biopsy procedure was standardized and the pathology report for PCa diagnosis was centralized and blinded for both urologists and the pathologist regarding clinical characteristics. The study also has some limitations, benign biopsies with cancer were taken from men that were not actually missed, since they had at least one positive biopsy. Ideally, we would investigate biopsies from men with only initially negative biopsies that developed cancer in follow-up data. While the well-controlled study design and histopathology image scanning protocol provides high quality data and opportunity to demonstrate the feasibility of the approach on the conceptual level, it does not provide demonstration of generalisability of the model to other study populations. Future studies would have to be focused on determining to what extent the model would allow generalisation to WSIs from additional pathology labs and images captured on other scanner hardware. In addition, the study sample used here was enriched by PCa with higher ISUP, which might also contribute to the observed higher sensitivity to detect men with high ISUP PCa from benign biopsies.

Conclusion

Subtle tumour-associated morphological changes in benign prostate tissue that cannot be distinguished by human eye can be captured by deep CNN models trained on large numbers of benign prostate biopsy histopathology images. The developed model has the ability to detect men with risk of missed prostate cancer after biopsy, caused by under-sampling of the prostate. The proposed model has the potential to reduce the number of false negative cases caused by sparse sampling of the prostate volume in routine systematic prostate biopsies and to indicate men that could benefit from re-biopsy.

References

1. Rawla. Epidemiology of Prostate Cancer. World J. Oncol. 2019
2. Prostatacancer.
3. EAU Guidelines: Prostate Cancer.
4. Shah *et al.* Prostate Biopsy Interpretation: An Illustrated Guide. 2012
5. Delongchamps *et al.* Saturation biopsies on autopsied prostates for detecting and characterizing prostate cancer. BJU Int. 2009
6. Haas *et al.* Needle biopsies on autopsy prostates: sensitivity of cancer detection based on true prevalence. J. Natl. Cancer Inst. 2007
7. Babayan *et al.* Biopsy Prophylaxis, Technique, Complications, and Repeat Biopsies. Prostate Cancer 2016
8. Sooriakumaran *et al.* Gleason scoring varies among pathologists and this affects clinical risk in patients with prostate cancer. Clin. Oncol. 2005
9. Hanahan *et al.* Hallmarks of Cancer: The Next Generation. Cell 2011
10. Partin *et al.* Clinical validation of an epigenetic assay to predict negative histopathological results in repeat prostate biopsies. J. Urol. 2014
11. LeCun *et al.* Deep learning. Nature 2015
12. Campanella *et al.* Clinical-grade computational pathology using weakly supervised deep learning on whole slide images. Nat. Med. 2019
13. Ström *et al.* Artificial intelligence for diagnosis and grading of prostate cancer in biopsies: a population-based, diagnostic study. Lancet Oncol. 2020
14. Bulten *et al.* Automated deep-learning system for Gleason grading of prostate cancer using biopsies: a diagnostic study. Lancet Oncol. 2020
15. Coudray *et al.* Classification and mutation prediction from non-small cell lung cancer histopathology images using deep learning. Nature Medicine 2018
16. Schmauch *et al.* A deep learning model to predict RNA-Seq expression of tumours from whole slide images. Nat. Commun. 2020
17. Kather *et al.* Deep learning can predict microsatellite instability directly from histology in gastrointestinal cancer. Nat. Med. 2019
18. Grönberg *et al.* Prostate cancer screening in men aged 50-69 years (STHLM3): a prospective population-based diagnostic study. Lancet Oncol. 2015
19. Epstein *et al.* The 2014 International Society of Urological Pathology (ISUP) Consensus Conference on Gleason Grading of Prostatic Carcinoma: Definition of Grading Patterns and Proposal for a New Grading System. Am. J. Surg. Pathol. 2016
20. Goode *et al.* OpenSlide: A vendor-neutral software foundation for digital pathology. J. Pathol. Inform. 2013
21. Otsu. A Threshold Selection Method from Gray-Level Histograms. IEEE Transactions on Systems, Man, and Cybernetics 1979
22. He *et al.* Deep residual learning for image recognition. in Proceedings of the IEEE conference on computer vision and pattern recognition (2016).
23. qubvel. qubvel/classification_models.
24. Russakovsky *et al.* ImageNet Large Scale Visual Recognition Challenge. Int. J. Comput. Vis. 2015
25. Kingma *et al.* Adam: A Method for Stochastic Optimization. arXiv [cs.LG] 2014
26. Srivastava *et al.* Dropout: a simple way to prevent neural networks from overfitting. J. Mach. Learn. Res. 2014
27. Selvaraju *et al.* Grad-cam: Visual explanations from deep networks via gradient-based localization. in Proceedings of the IEEE international conference on computer vision (2017).
28. McInnes *et al.* UMAP: Uniform Manifold Approximation and Projection for Dimension Reduction. arXiv [stat.ML] 2018
29. Djavan *et al.* Predictability and significance of multifocal prostate cancer in the radical prostatectomy specimen. Tech. Urol. 1999

30. Carlsson *et al.* Current routines for transrectal ultrasound-guided prostate biopsy: a web-based survey by the Swedish Urology Network. *Scand. J. Urol. Nephrol.* 2012
31. Chun *et al.* Optimizing performance and interpretation of prostate biopsy: a critical analysis of the literature. *Eur. Urol.* 2010
32. Pepe *et al.* Saturation prostate needle biopsy and prostate cancer detection at initial and repeat evaluation. *Urology* 2007
33. Lane *et al.* Saturation technique does not decrease cancer detection during followup after initial prostate biopsy. *J. Urol.* 2008
34. Kawakami *et al.* History of malignancy is a predictor of prostate cancer detection: incorporation into a pre-biopsy nomogram. *Int. J. Urol.* 2008
35. Kawamura *et al.* Development of a new nomogram for predicting the probability of a positive initial prostate biopsy in Japanese patients with serum PSA levels less than 10 ng/mL. *Int. J. Urol.* 2008
36. Mcneal *et al.* PATTERNS OF PROGRESSION IN PROSTATE CANCER. *Lancet* 1986
37. Schröder *et al.* Prostate-cancer mortality at 11 years of follow-up. *N. Engl. J. Med.* 2012
38. Contemporary approach to active surveillance for favorable risk prostate cancer. *Asian Journal of Urology* 2019
39. Sathianathen *et al.* Landmarks in prostate cancer. *Nat. Rev. Urol.* 2018
40. Lucas *et al.* Deep learning for automatic Gleason pattern classification for grade group determination of prostate biopsies. *Virchows Arch.* 2019
41. Nir *et al.* Automatic grading of prostate cancer in digitized histopathology images: Learning from multiple experts. *Med. Image Anal.* 2018
42. Arvaniti *et al.* Automated Gleason grading of prostate cancer tissue microarrays via deep learning. *Sci. Rep.*

Supplementary materials

Image pre-processing

Tissue segmentation

We first generated tissue masks separating the prostate tissue from the background. The images were read at full resolution (0.4536 μm /pixel), downsampled by 2^5 from the 20X images using the resolution pyramid from OpenSlide (v. 1.1.1)¹. Next, we converted the RGB images to HSV encoded images using the color module in scikit-image (v.0.14.2)². Tissue areas were defined as regions above the Ostu's threshold in saturation and above 0.75 threshold in hue, background areas were discarded from further analysis. In addition, pen marks were present in a small number of benign slides, which marked suspicious regions for cancer or PIN. The pen marks were filtered out from the tissue areas using the following functions from OpenCV (v.3.4.2)³: first, the RGB channel was converted to grayscale using `COLOR_BGR2GRAY()`; second, a "2D" Laplacian operator was applied using `Laplacian()` with the Sobel kernel size of three and depth of the output image size set as `CV_16S`; last, the absolute value of the resulting response was obtained using `convertScaleAbs()` and the pen marks subsequently filtered if below the threshold 20 of the absolute value. We further smoothed tissue masks (removing peppers and salts) by applying a morphological opening and closing, with a disk with a radius of 6 using functions of `disk()`, `opening()`, and `closing()` in scikit-image morphology module⁴.

Image tiling and quality control

To facilitate model training, WSIs were tiled into small image patches. We used a window size of 598×598 pixels from the 20X full resolution (0.4536 μm /pixel) and a stride of 299 pixels. The tiles were subsequently downsampled by a factor of 2, the resulting image patches are of size 299×299 pixels and with 50% overlap between the adjacent tiles. Tiles that didn't contain more than 20% of tissue were excluded. To ensure the quality of the images, we excluded unsharp tiles due to poor focusing during scanning. We calculated the variance after the Laplacian filter using `variance_to_laplacian()` function in OpenCV³ and excluded tiles with the variance lower than 200.

Model development

Model overview

We randomly split the dataset on the man level into training (973 men), validation (238 men), and held-out test

(297 men) sets. Training and validation sets combined, and the held-out test, were balanced on PCa diagnosis, age, PSA, and further balanced on ISUP for PCa patients. The validation set was used only once to validate final model performance, and the held-out test was only used once to evaluate final model performance. We used the ResNet-18^{5,6} with weights initialized from a model pre-trained by ImageNet⁷ images as the base model. A dropout layer of the 50% chance was added after the global average pooling of the last convolutionation layer from the base model. This output layer was subsequently concatenated with categorical covariates of age (≤ 55 , 55- 60, 60-65, 65-70, 70-100 years) and PSA (1-3, 3-5, 5-10, ≥ 10 ng/ml). We additionally included a fully connected layer to 256 hidden units allowing potential interactions among age, PSA and the learned image features. Max norm regularization was applied.

Model training

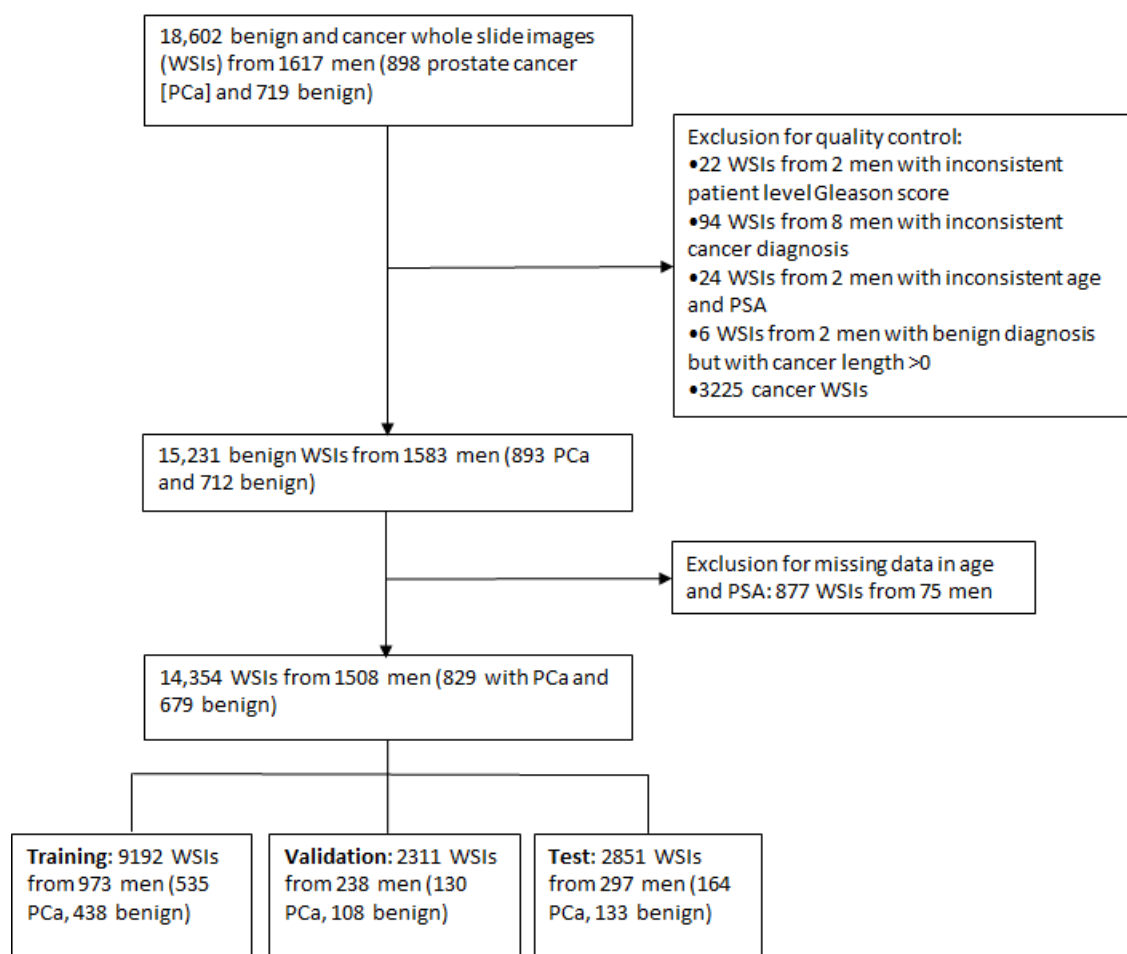
Parameters from all layers were optimized by backpropagation through mini-batch stochastic gradient descent (SGD) and binary cross-entropy loss. Learning rates of $1e-5$, $1e-6$, and $1e-7$ were first evaluated using 5-fold cross validation in the training set, and $1e-5$ was selected as the learning rate for subsequent optimisations and analyses. The initial learning rate of $1e-5$ was reduced by 50% if loss function stopped improving (measured by minimum change of 0.0001) for consecutive 35 epochs. We applied the standard data augmentation including rotation and flip. In order to reduce overfitting, for each fold, the training set was splitted into training, tuning, and inner validation sets, which ensured that the best model was selected based on the performance in the tuning set and model performance was validated in the inner validation set.

To improve the model generalization, we used an ensemble of 10 CNN models sharing the same model architecture and hyperparameters, while the variability within the ensemble arises from the stochastic sampling during training. For training, at each step we randomly sampled a mini-batch of 170 images with equal proportion of image tiles from PCa and non-PCa groups. During optimization we defined 300 iterations as one ‘partial epoch’, after which the tuning set was evaluated. We allowed a maximum of 400 partial epochs and used an early-stopping with patience of 35 epochs. Less than a minimum change in loss of 0.0001 was considered as no improvement.

Model prediction and model interpretation

The final model prediction performance was only validated once in the validation set (**eFigure 1** and **eTable 2**) and

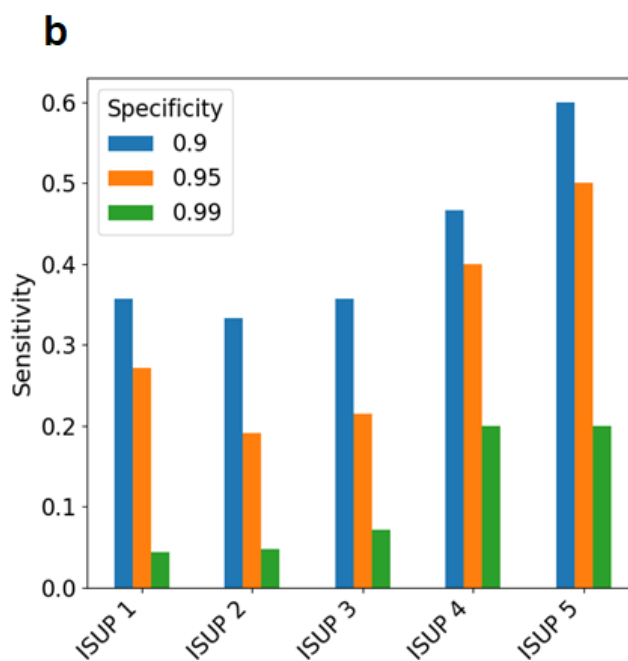
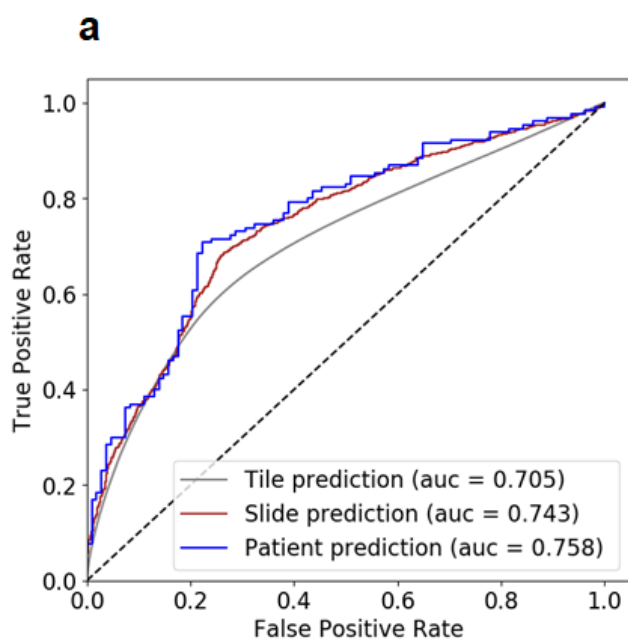
only tested once in the held-out test set. Tile level predictions in the validation and test sets were obtained by averaging of the prediction scores from the ten-model ensemble. Slide level predictions were calculated using the 75% percentile of the tile level prediction distribution. A patient level prediction was aggregated using the median of the slide level prediction score. For model interpretation, we selected the model with the highest tile level AUC obtained in the testset. We randomly selected 20% tiles in the test set stratified by PCa diagnosis and generated 2-D UMAP from the modelled 512-dimensional feature vector using the “umap-learn”⁸ with parameters set to `n_neighbors=15, min_dist=0.1, n_components=2, metric='euclidean'`. Through visualization of the UMAP, we selected four distinct regions for PCa patients and healthy men representing characteristic morphological structures learned from CNN. For each region, we generated GradCam visualizations for 16 tiles with the highest prediction score among PCa patients and 16 tiles with the lowest prediction among healthy men to visualize the morphological patterns linked to PCa prediction.



eFigure 1. Flow-chart

eTable 1 Sensitivity by ISUP according to different specificity levels in held-out test set

Specificity	Sensitivity				
	ISUP 1	ISUP 2	ISUP 3	ISUP 4	ISUP 5
0.99	0.01	0.03	0.08	0.09	0.10
0.95	0.19	0.16	0.17	0.31	0.40
0.90	0.28	0.31	0.33	0.41	0.70



eFigure 2. Prediction performance in validation set a) Receiver Operating Characteristic (ROC) curves and associated AUC estimates in the validation set for prediction of cancer versus benign PCa diagnosis on tile, slide, and patient level; b) corresponding sensitivity by ISUP group at specificities of 0.99, 0.95, and 0.90.

eTable 2 Sensitivity by ISUP according to different specificity levels in validation set

Specificity	Sensitivity				
	ISUP 1	ISUP 2	ISUP 3	ISUP 4	ISUP 5
0.99	0.04	0.05	0.07	0.20	0.20
0.95	0.27	0.19	0.21	0.40	0.50
0.90	0.36	0.33	0.36	0.47	0.60

Reference

1. Goode *et al.* OpenSlide: A vendor-neutral software foundation for digital pathology. J. Pathol. Inform. 2013
2. van der Walt *et al.* scikit-image: image processing in Python. PeerJ 2014
3. BRADSKI *et al.* The OpenCV library. Dr Dobb's J. Software Tools 2000
4. Module: morphology — skimage v0.14.3 docs.
5. He *et al.* Deep residual learning for image recognition. in Proceedings of the IEEE conference on computer vision and pattern recognition (2016).
6. qubvel. qubvel/classification_models.
7. Deng *et al.* ImageNet: A large-scale hierarchical image database. 2009 IEEE Conference on Computer Vision and Pattern Recognition 2009
8. UMAP: Uniform Manifold Approximation and Projection for Dimension Reduction — umap 0.5 documentation.